Impact of windflow calculations on simulations of alpine snow accumulation, redistribution and ablation

Impact of windflow calculations on simulations of alpine snow accumulation, redistribution and ablation

K. N. Musselman[1*], J. W. Pomeroy[1], R. L. H. Essery[2], and N. Leroux[1]

[1] Centre for Hydrology, University of Saskatchewan, Saskatoon, SK Canada
[2]School of GeoSciences, University of Edinburgh, Edinburgh, UK
*Corresponding author; email: keith.musselman@usask.ca

ABSTRACT

Wind redistribution, radiation and turbulent heat fluxes determine seasonal snow accumulation and melt patterns in alpine environments. Mathematical representations of windflow vary in complexity and introduce uncertainty to snow modelling. To characterize this uncertainty, a spatially distributed snow model that considers the physics of blowing snow transport and sublimation and the energy fluxes contributing to snowpack ablation was evaluated for its ability to simulate seasonal snow patterns around a windy alpine ridge in the Canadian Rockies. The model was forced with output from three windflow models of varying computational complexity and physical realism: i) a terrain-based empirical interpolation of station observations, ii) a simple turbulence model, and iii) a computational fluid dynamics model. Compared to wind measurements, the windflow simulations produced similar and relatively accurate (biases lower than ± 1.1 m s^{-1}) wind speed estimates. However, the snow mass budget simulated by the snow model was highly sensitive to the windflow simulation used. Compared to measurements, distributed snow model depth and water equivalent errors were smallest using either of the two turbulence models, with the best representation of downwind drifts by the computational fluid dynamics model. Sublimation was an important mass loss from the ridge and windflow model choice resulted in cumulative seasonal sublimation differences ranging from 10.5% to 19.0% of seasonal snowfall. When aggregated to larger scales, differences in cumulative snowmelt and snow transport were negligible but persistent differences in sublimation and snow-covered area suggest that windflow model choice can have significant implications at multiple scales. Uncertainty can be reduced by using physically based windflow models to drive distributed snow models.

Keywords: blowing snow, wind, windflow model, alpine snow, sublimation

1. INTRODUCTION

The evolution of an alpine snowpack is greatly influenced by wind patterns. During and after snowfall events, wind can redistribute snow from exposed areas and deposit it in sheltered regions (Pomeroy *et al.*, 1997; Essery and Pomeroy, 2004). In the absence of vegetation, topography and cumulative synoptic wind patterns determine the formation and persistence of snow drifts in alpine environments (Greene *et al.*, 1999; Mott *et al.*, 2010; Schirmer *et al.*, 2011) with important ecohydrological impacts (Williams and Melack, 1991; Brooks and Williams, 1999; Walker *et al.*, 2001; Wipf *et al.*, 2009). Particularly in mid-winter, turbulent energy exchange at the snow surface can exceed radiation in importance and result in sublimation losses (Marks and Dozier, 1992; Marks and Winstral, 2001). In cold, dry and windy environments, the additional sublimation of blowing snow can be a substantial fraction of winter snowfall (Pomeroy, 1989). During wind transport through an unsaturated atmosphere, snow particles are well ventilated and undergo sublimation at rates exceeding that of the snow surface (Dyunin, 1959; Schmidt, 1972; Schmidt, 1986). Sublimation losses are important to consider in cold

regions hydrological models and estimation requires accurate windflow representation (Bowling *et al.*, 2004).

Windflow also has important effects on snowmelt rates. Wind affects the spatial patterns of meltwater availability indirectly through its influence on the end-of-winter snow distribution (Pomeroy *et al.*, 1998; Pomeroy *et al.*, 2003; Grunewald *et al.*, 2010; Schirmer *et al.*, 2011; Egli *et al.*, 2012) and directly through the turbulent exchange of temperature and water vapor between the snow surface and the overlying air (Male and Granger, 1981). Pohl *et al*. (2006) and Menard *et al*. (2014) have shown that variable wind exposure over complex terrain strongly influences turbulent transfer to snow and subsequent melt rates.

In mountainous terrain, windflow patterns exhibit complex variability at spatial scales that complicate efforts to map the influence of topography on wind speed and direction. Many models rely on terrain-based empirical calibration on available measurements (e.g., Liston and Sturm, 1998) or terrain shelter parameterizations based on assumed mean flow fields (e.g., Winstral and Marks, 2002). Linearized turbulence models such as the MS3DJH/3R model (Walmsley *et al.*, 1982; Taylor *et al.*, 1983; Walmsley *et al.*, 1986) have been used to drive a distributed blowing snow model (Essery *et al.*, 1999; Fang and Pomeroy, 2009). Linear turbulence models represent windflow in a more physically realistic manner than the terrain-based methods, but the simplified physics limits application to gentle slopes. More recently, computationally intensive nonlinear turbulence models with stronger physical realism have been used to downscale windflow patterns simulated by atmospheric models to simulate snow-drift processes in complex terrain (Lehning *et al.*, 2008; Mott *et al.*, 2008; Bernhardt *et al.*, 2009; Dadic *et al.*, 2010; Mott and Lehning, 2010). The approaches highlight a disparity in model complexity in how windflow is commonly calculated in distributed snow model studies.

The objective of this paper is to explore warranted model complexity (Dornes *et al.*, 2008) for calculating seasonal snowpack evolution around an alpine ridge and to examine how different windflow representations can propagate errors when used to drive a distributed blowing snow and energy balance model. The study examines the impact of windflow calculations on simulations of alpine snow redistribution, sublimation and subsequent melt; however, as in most energy balance snow models, the turbulent advection from heterogeneous surface heating is not considered. Specific research questions include: i) what is the relative accuracy of three windflow models of varying computational complexity and physical realism? ii) how sensitive are the snow mass balance calculations of a distributed blowing snow and energy balance model to the representation of windflow? iii) do differences in snow dynamics calculated using different windflow models persist as time and space scales increase?

2. METHODS

2.1. Study site and measurements

Fisera Ridge is an alpine study site in the Marmot Creek Research Basin (50°57'N; 115°12'W), in the Canadian Rocky Mountains, Alberta, Canada (Figure 1). The site is located near treeline at 2320 m above sea level (asl) and the land cover is primarily bare soil and alpine grasses. The

ridge has an E-NE orientation and a generally perpendicular W-NW prevailing wind (Figure 2). Any winter snow deposition on the windward (NW) slope is quickly wind-scoured and deposited in a ~100 m zone on the leeward (SE) slope downwind of the ridge crest. The leeward and windward slopes are < 20° and the ridge crest is rounded with a gradual change in slope (i.e., terrain curvature).

Three meteorological stations were located on the windward slope (windward station), the top of the ridge (ridgetop station), and the leeward slope (leeward station) over a ~160 m linear distance (Figure 1). The ridgetop station was located midway between the two stations and slightly offset down the ridge crest (Figure 1). The ridgetop station recorded 15-minute averages of 10-second measurements of air temperature and relative humidity (Campbell Scientific® HMP45C212 probe with a Gill radiation shield at a height of 2.3 m), incoming shortwave and longwave radiation (Kipp & Zonen® CNR1 net radiometer at a height of 1.4 m), snow depth (Campbell Scientific® SR50-45 ultrasonic sensor), and wind speed and direction (R.M. Young® 05103AP at a height of 2.6 m). Snow depth (SR50-45) and wind speed were also recorded at the windward and leeward stations with Met One® 013 three-cup anemometers at heights of 2.4 m (windward) and 3.2 m (leeward). The nearest precipitation measurement was from a shielded Geonor T200B gauge two km away in a forest clearing at 1845 m asl. After the study, an identical gauge was installed in a sheltered area near the ridgetop station. The relationship between precipitation values measured at the two locations for the 2009 water year was used to estimate a multiplicative increase with elevation (1.86) to extrapolate measurements to the Fisera Ridge study plot. Precipitation measurements were corrected for gauge under-catch as in MacDonald *et al.* (2010). When air temperature was ≤ 0°C, relative humidity was estimated with respect to ice following Yang *et al.*, (2010).

Thirteen manual snow surveys of depth and density were conducted between late-January and May of 2008. Surveys consisted of two bisecting transects: a slope-parallel transect extended from the windward station over the ridge and down beyond the leeward station and a shorter ridge crest transect that extended below the ridgetop station (Figure 1). Snow depth was measured every 1 - 3 m and snow density was measured every fifth depth measurement using an ESC-30 snow tube and handheld spring scale when snow depth permitted (~20 cm < depth < ~120 cm). Otherwise, depth-integrated density measurements (1000 cm^3) were made at snowpits near the automated stations. Snow density values from the nearest measurement location were used to estimate SWE from survey depth measurements.

Airborne light detection and ranging (LiDAR) mapping was conducted in August, 2007 (snow-free) and again on 28 March, 2008 (snow-covered). A digital elevation model (DEM) and a snow depth model at one-metre resolution were created from the data (Hopkinson *et al.*, 2012). The aerodynamic surface roughness length estimated from LiDAR-derived vegetation height and land surface classification is provided in Figure 1 (see Section 2.3.3). Note that the ridge and immediate slopes are unvegetated to sparsely-vegetated.

2.2. Snow model

Meteorological observations from the ridgetop station were used to force a physically based snow redistribution, mass and energy balance model at 8 m grid spacing over a 1.024 km by 1.024 km model domain centred on the Fisera Ridge study area (Figure 1). The average slope within the domain was 22° ± 7° with a maximum slope value of 52°. The Distributed Snow Model (DSM) is a multi-layer soil and three-layer snow model that considers blowing snow and in-transit sublimation based on a simplified version (Essery et al., 1999) of the Prairie Blowing Snow Model (PBSM) (Pomeroy *et al.*, 1993; Pomeroy and Li, 2000). The snowpack compaction and thermodynamic routines are based on the JULES land surface model (Best *et al.*, 2011). The soil routine is described in Ménard et al. (2014). Meteorological observations other than wind speed and slope-projected shortwave radiation were assumed to be homogeneous. The windflow and blowing snow models were not fully coupled in that surface roughness (0.005 m) did not change with snow depth.

Wind speed variation due to topography was estimated with three different windflow models of varying computational complexity and physical realism (see Section 2.3). The windflow models produced maps of wind speed normalized by the ridgetop station values for eight wind directions. For each direction, normalized windflow maps were provided as a library to DSM to estimate wind speed over the domain from the measured wind speed and direction at the ridgetop station.

2.3. Windflow models

2.3.1. 'Liston-Sturm' empirical windflow model

The simplest of the three windflow models evaluated, an empirical model by Liston and Sturm (1998) (hereafter LS) was used with point wind speed and direction observed at the ridgetop station in conjunction with wind-topography relationships to extrapolate wind speed to grid cells. While the full LS model includes a diverting algorithm (Ryan, 1977) to estimate terrain-induced wind direction, the wind direction measured at the ridgetop station was uniformly applied to all grid cells for consistency with DSM assumptions. Terrain curvature, slope, and aspect were computed from the DEM following Liston and Sturm (1998). The average terrain curvature in four directions was computed with a 50 m length scale; estimated to be the average distance between the ridge crest and the middle of the two slopes, or approximately half the wavelength of Fisera Ridge. The upwind slope was computed for eight primary wind directions. For each grid cell (i,j) and wind direction (θ) a wind weighting factor, $W_{w_{i,j,\theta}}$, used to modify the measured wind speed, was estimated from the upwind slope ($\Omega_{s_{i,j,\theta}}$) and curvature ($\Omega_{c_{i,j}}$) terrain parameters, both scaled such that $-0.5 \leq \Omega_{s,c} \leq 0.5$, as in (Liston and Sturm, 1998):

$$W_{w_{i,j,\theta}} = 1 + \gamma_s \Omega_{s_{i,j,\theta}} + \gamma_c \Omega_c \qquad (1)$$

where the additional upwind slope and curvature weighting factors (γ_s and γ_c) with a range of [0,1] were specified as 0.5 to equally weight the importance of the two terrain parameters in determining the local windflow around Fisera Ridge; this value is close to that determined

empirically in Liston and Elder (2006). The eight wind weight maps were provided as input to DSM as described in Section 2.2.

2.3.2. Mason-Sykes turbulence windflow model

The second windflow model evaluated was a simple linear turbulence model developed from the two-dimensional theoretical work of Jackson and Hunt (1975) by Walmsley *et al.* (1986) and applied to three-dimensional (3-D) topography as in Mason and Sykes (1979) (hereafter, MS). It solves linearized momentum equations using Fourier transforms of the topography. The model offers more theoretical and physical realism than the empirical LS model, but does makes a number of simplifying assumptions, including neutral stratification, and as a result it is only valid over low hills (slopes < 25%). The MS model was run over the domain with a constant roughness length of 0.005 m as in Essery *et al.* (1999). The model produced normalized wind speed tables for the primary wind directions.

2.3.3. Windsim® windflow model

The third and most physically based windflow model examined was the commercial Windsim® computational fluid dynamics (CFD) package (http://windsim.com) designed for the assessment of wind energy resources in complex terrain. The CFD windflow model (hereafter WS), is based on a 3-D Reynolds Averaged Navier Stokes (RANS) solver and uses a k - ε turbulence closure scheme (Launder and Spalding, 1974). By solving the non-linear transport equations for mass, momentum and energy, WS offers more theoretical and physical realism than the (linear) MS turbulence model and may therefore be a more suitable windflow model in mountainous terrain. A nesting technique was used to define the lateral boundary conditions of the (inner) 1.024 km x 1.024 km model domain. A 24 km x 24 km (outer) domain at 120 m horizontal resolution was defined (Figure 1). The upper boundary conditions for both domains were specified with the 'constant pressure' boundary option in WS, described to be most suitable for complex terrain. The lateral boundary conditions of the outer domain were specified with a logarithmic velocity profile < 500 m above the terrain; above this height a constant wind profile and 20 m s^{-1} geostrophic wind speed was specified. The surface roughness of the outer domain was estimated as a function of terrain elevation (Gravdahl and Vargvei, 1998). The logarithmic profile assumption is only valid over flat terrain, which is violated here, but was only used to specify the lateral boundary conditions of the outer domain to estimate the inner domain wind profile. The nested domains were vertically discretized into 50 layers of 10 m thickness except for the lowest layer, which was prescribed a 6 m thickness extending to 4 m above the DEM surface. Experiments conducted with minimum heights < 4 m produced physically inconsistent values indicative of numerical solution issues (not shown). Surface roughness lengths over the inner domain (Figure 1) were estimated from vegetation height, h, derived from LiDAR measurements. Roughness lengths for the inner WS simulations were specified as $0.5h$ for $h \geq 2$ m, $0.4h$ for $0.4 \leq h < 2.0$, and a minimum of 0.005 or $0.1h$ for $h < 0.4$ (Wallace and Hobbs, 2006). The specification of LiDAR-derived roughness lengths might be expected to improve

windflow performance over the two simpler models that either did not consider terrain roughness (LS) or that considered the roughness length to be constant (MS).

The WS windflow model produced orthogonal *u*, *v*, *w* wind speed vector components for each primary wind direction and specified height. Results from a height of 4 m above the inner domain (snow-free) surface were used. For each wind direction, the horizontal wind speed was calculated and the resulting wind field was normalized by the wind speed simulated at the pixel corresponding to the location of the ridgetop station.

2.4. Experimental design

2.4.1. Windflow model evaluation against measurements

The three windflow models were evaluated for their relative skill at simulating the observed wind speed on opposing slopes of the Fisera Ridge site. Windflow model accuracy was evaluated against 15-minute data (n=57,441) for the October, 2008 to September, 2010 period when wind data were available from all three stations. For each time step and windflow model, the ridgetop station wind direction was used to reference the corresponding windflow map. The simulated (normalized) wind speed values at locations of the windward and leeward stations were then multiplied by the wind speed measured at the ridgetop station. The model root mean squared error (RMSE) and bias values were computed. In addition, the modelled and measured wind speed values were evaluated for time steps when the wind was out of the prevailing W-NW direction, or roughly perpendicular to Fisera Ridge.

2.4.2. Assessment of the impact of windflow calculation on simulated snowpack states

Snow depth and SWE estimates from DSM forced by output from the three windflow models were evaluated against multi-scale snowpack measurements. At the point-scale, simulated (daily) snow depth values at the locations of the three stations were compared to automated measurements. Modelled SWE was evaluated against field-based estimates derived from thirteen (manual) snow density measurements and coincident (automated) snow depth measurements. At the slope-scale, model simulations of SWE along the 'T-shaped' survey transect were evaluated against survey measurements using nearest-neighbor averaging. Results for each windflow model and for the respective transect-slope (i.e., windward, ridgetop, and leeward) are reported in terms of the mean and standard deviation of the SWE error ('modelled minus measured'). In addition, spatially explicit snow depth simulations for 28 March, 2008 were qualitatively compared to LiDAR-derived snow depth resampled from 1 m to 8 m grid spacing. Finally, the impacts of the three windflow calculations on both the magnitude and timing of slope-averaged simulated snow mass fluxes were evaluated. Simulated snow-covered area (SCA) and cumulative seasonal snow transport, surface and blowing snow sublimation, and melt fluxes were compared amongst the three windflow models. To evaluate whether different windflow calculations impact the relative timing of simulated snow transport and sublimation, the normalized and cumulative frequency of the hourly fluxes were binned into 12-hours periods relative to the last precipitation event and the distributions were compared.

3. Results

The perpendicular orientation of Fisera Ridge to the prevailing wind direction (290°; Figure 2) resulted in high measured wind speeds at the exposed windward and ridgetop station locations with lower wind speeds on the sheltered leeward side. The average and standard deviation of the 15-minute wind speed measured at the windward, ridgetop, and leeward stations between 1 October, 2007 and 30 September, 2010 were 3.1 ± 2.6 m s^{-1}, 2.3 ± 2.2 m s^{-1}, and 2.3 ± 1.5 m s^{-1}, respectively. The pronounced wind speed variability over relatively short distances (~100 m) is typical of windflow patterns in complex alpine terrain.

The three windflow models used to simulate wind speed on the opposing slopes produced reasonable results compared to one year of measured wind speed (Figure 3). The RMSE and bias values for all models were < 1.7 m s^{-1} and better than ±1.1 m s^{-1}, respectively (Figure 4). Model errors were generally similar as indexed by the correlation coefficients (Figure 3) and RMSE values (Figure 4). The LS model slightly overestimated wind speed on both the leeward and windward slopes (Figures 3 and 4). The MS model also underestimated wind speed on both slopes and was the only model with negative wind speed biases (Figures 3 and 4). The WS model exhibited near-zero mean model biases (Figure 4), but was prone to overestimating high wind speeds (Figure 3).

Automated and manual snow measurements indicated that both the windward and ridgetop sites were largely wind-scoured with seasonal average snow depths around 20 cm (Figure 5). The deepest snowpack accumulated on the wind-exposed slopes during a series of spring snowfall events when wet snow conditions restricted wind erosion (April - June). In contrast to the wind-scoured slopes, a large drift accumulated on the leeward slope where snow depths ranged between 100 and 180 cm and SWE exceeded 600 mm (Figure 5). At all sites, maximum SWE occurred in early-May.

DSM forced by the three windflow models produced distinct differences in the seasonal evolution, magnitude and location of simulated snow drifts (Figure 5). All DSM runs simulated the mid-winter scour of the windward slope quite well, although the late-spring accumulation events were uniformly overestimated. Compared to depth and SWE measurements at the windward station, the MS turbulence model resulted in the lowest RMSE and bias values while the empirical LS model, and particularly the CFD WS windflow model, caused overestimated accumulation on the wind-exposed slope (see Table 1). At the ridgetop station, greater differences in depth and SWE were simulated amongst the three model runs (Figure 5). As on the windward slope, the MS-driven DSM best represented the frequent wind-scour of snow at the ridgetop station with small depth and SWE biases of +3.5 cm and +11 mm, respectively (Table 1). Conversely, the LS-driven DSM erroneously simulated a large drift near the ridgetop station with large depth and SWE biases of +73.9 cm and +419 mm, respectively (Figure 5 and Table 1). All DSM runs simulated drift formation on the leeward slope, but generally underestimated the magnitude. The WS-driven DSM was closest to accurately simulating the leeward drift, with depth and SWE biases of -10 cm and -66 mm, respectively (Figure 5 and Table 1). The MS- and LS-driven DSM runs significantly underestimated the leeward SWE with mean biases of -157

mm and -259 mm, respectively. In general, improved SWE estimation was obtained with the more physically based windflow models (MS and WS).

To better understand the cause of the simulated snowpack differences as determined at the individual stations, the following metrics were evaluated along the 160 m linear transect between the windward and leeward stations: 1) modelled wind speeds in the prevailing wind direction (290°) relative to that measured at the ridgetop station (Figure 6a), 2) the change in the modelled wind speed with distance du/dx (Figure 6b) and 3) the simulated SWE (Figure 6c) over the ridge transect elevation profile (Figure 6d). The WS and LS models simulated a decrease in wind speed from the windward to leeward sides while the MS model simulated wind speeds on the ridgetop and windward slope, but a greater leeward decline in wind speed than the other two models. Comparatively, the LS model simulated a relatively smooth wind speed transition from the windward to leeward slopes. Breaks in the wind speed slope were greater in the two turbulence models than the LS windflow model, but were simulated in different locations along the ridge transect (Figure 6b). DSM modelled SWE (Figure 6c) varied significantly along the ridge transect and that variability was windflow-model dependent. In general, DSM forced by the two turbulence models simulated the greatest SWE on the leeward slope with DSM forced by the WS model simulating the drift slightly closer to the ridgetop on the leeward side than the MS-driven model. DSM forced by the empirical LS model erroneously simulated this drift slightly to the windward side of the ridge.

Compared to the 28 March LiDAR snow depth estimates, the greatest differences in the snow depth patterns from DSM forced by the three windflow models were amongst the empirical LS model and the two turbulence models (Figure 7). The LS model resulted in a smoothly varying snow-cover, deepest in proximity to the ridge crest and shallowest on both the windward and leeward slopes. This is in contrast to the general understanding of snow accumulation around alpine ridges (Pomeroy and Gray, 1995). By comparison, the two turbulence models resulted in snow-cover patterns that were similar to the LiDAR derived snow cover with shallow snow and snow-free areas on the windward and ridgetop zones, and deep and spatially heterogeneous drifts covering much of the leeward slope. DSM forced by the two turbulence models simulated the deepest snowpack (> 200 cm) in roughly similar locations, with the WS-driven DSM simulated drift forming slightly closer to the ridge crest than the MS-driven model as described in the transect evaluation. Note that the LiDAR product indicates deep drifts around small trees in the southern- and eastern-most parts of the domain (see roughness heights in Figure 1); these areas are included in the LiDAR depth map for completeness, but the inclusion of sparsely vegetated areas prevents direct quantitative comparison of the measured and modelled products because the DSM does not include vegetation roughness impacts on snowpack distribution and ablation.

Time-series of the seasonal evolution of simulated SWE is provided in Figure 8. Notably, the 29 April snow-cover extent is greater than the mid-winter distributions as a result of wetter spring snow conditions and an associated lower likelihood of wind transport (Li and Pomeroy, 1997); this dynamic is recorded in the observations (Figure 5) and is generally captured by DSM regardless of the windflow model.

Slope- and windflow model-specific SWE errors, computed as the seasonal average error against data from the 13 snow surveys, show the general overestimation of SWE on the windward slope and ridgetop by the LS-driven DSM (299±135 mm and 311±123 mm, respectively) and, to a lesser extent, by the WS-driven DSM (138±98 mm and 142±91 mm, respectively) (Figure 9). DSM forced by the MS turbulence model outperformed SWE estimated by DSM forced by the other two windflow models at the two wind-exposed areas (35±59 mm and -23±75 mm, respectively). On the leeward side of Fisera Ridge, DSM forced by any windflow model underestimated SWE, but the WS model had significantly reduced errors (-28±91 mm) relative to DSM driven by the LS (-114±97 mm) and MS (-131±86 mm) windflow models (Figure 9).

Differences in the impact of windflow calculations on snow regime estimation (i.e., depth and SWE) were largely manifested in how the windflow models impacted the calculation of seasonal snow fluxes including transport and sublimation. The greatest concurrence in simulated transport, sublimation, melt, and SCA amongst the simulations forced by the three windflow models occurred for the leeward slope (Figure 10), where wind speeds were lowest by all estimates (Figure 2). The greatest deviation in cumulative blowing snow transport and sublimation due to the windflow model occurred at the ridgetop station, where the MS-driven DSM, found to be most accurate in terms of depth and SWE, generated the greatest snow transport (out) and the highest sublimation fluxes. The WS- and LS-driven DSM simulated ~50% and ~25%, respectively, of the cumulative seasonal (total) sublimation losses calculated by the MS-driven DSM. Only the LS model at the ridgetop station resulted in cumulative transport estimates that differed in sign from the other models in that snow accumulated at the ridgetop; the other model runs transported the snow off the ridgetop to the leeward slope.

The location of the greatest (total) sublimation losses was windflow model-dependent: sublimation was highest on the windward slope with the LS- and WS-driven DSM, but on the ridgetop with the MS-driven DSM (Figure 10). On average, cumulative surface sublimation losses were approximately 50% of the cumulative blowing snow sublimation losses. Blowing snow sublimation, reported as a percentage of cumulative seasonal snowfall, ranged from 8% (leeward station) to 20% (windward and ridgetop stations). On average across the three slopes (windward, ridgetop, and leeward rectangles in Figure 1), blowing snow sublimation losses with the MS and WS models were 19% and 17.5% of cumulative seasonal snowfall, respectively, while the average loss with the LS windflow model was only 10.5%. The sublimation source also exhibited seasonality; blowing snow sublimation generally ceased at the beginning of March, while most of the seasonal surface sublimation occurred from March through July (Figure 10). Blowing snow sublimation estimated by DSM forced with the two turbulence windflow models were similar to those in MacDonald et al. (2010) (19%) using the Cold Regions Hydrological Model for the same year and at the same site but forced by measured rather than simulated wind speeds.

To put the DSM results into context with those of model studies that treat blowing snow sublimation as a self-limiting mechanism, the meteorological observations and DSM blowing

snow sublimation estimates from the largest blowing snow event of the 2008 winter are provided (Figure 11). The event substantially redistributed alpine snow as is evident in the before and after photographs. For simplicity, only results from DSM forced with the WS windflow model are included in Figure 11. Following a period of light snow, low temperatures (-5° to -10°C), low wind speeds (1 m/s), and saturated relative humidity with respect to ice (100%) on the morning of Feb. 28, the snowfall stopped, air temperature plateaued at -4°C, relative humidity dropped to ~60%, and wind speed steadily increased (Figure 11). Two (hourly-average) wind speed maxima were measured on Feb. 29: one at 01:00 (15 m/s) and the other at 07:00 (19.5 m/s). The DSM simulated minor blowing snow fluxes (< 3.3 mm/hr; < 2 hrs.) corresponding to the timing of the first wind speed maxima before a more substantial blowing snow event lasting ~4 hrs. with maximum sublimation estimates of 13.3 mm/hr, 5.8 mm/hr, and 1.9 mm/hr on the windward, ridgetop, and leeward sides, respectively occurring at 08:00 on Feb. 29 (Figure 11). Simulated blowing snow sublimation stopped after four hours (10:00) and the wind speed dropped below 15 m/s. The air temperature measured at the ridgetop station steadily increased from -4.4°C at the beginning of the large blowing snow event (05:00 Feb. 29) to -1.7°C (10:00) and the relative humidity dropped slightly from 64% (05:00) to a minimum of 55% during the simulated blowing snow maximum (08:00) and increased to 59% by the end of the event (10:00) (Figure 11).

Early in the melt period, cumulative snowmelt was insensitive to windflow representation, and only became sensitive late in the season as differences in SCA depletion among the models dictated meltwater availability (Figure 10). The leeward slope generally had the greatest SCA with the latest snow-cover depletion, while the wind-scoured windward slope sustained an intermittent snow-cover (Figure 10). The LS model resulted in the smoothest and most homogeneous snow-cover (Figure 7) as well as the greatest SCA and latest snow-cover depletion on all slopes. In contrast, the MS model resulted in the most variable SCA and the WS model caused a gradual SCA change from intermittent (windward) to complete (leeward).

The results show that the windflow model choice can have significant implications for snow regimes and snow fluxes at point- to slope-scales. When averaged over the full model domain the differences in transport and melt were subtle to negligible; however, more appreciable differences in sublimation and snow-cover depletion suggest that windflow model choice can have important implications at multiple scales (Figure 10; right-most column). The windflow model choice not only influenced the magnitude of seasonal blowing snow transport and sublimation fluxes, but also the timing of these fluxes relative to snowfall events. In general, DSM simulated a large majority of seasonal (hourly) blowing snow transport to occur between 13 and 24 hours after a snow event (Figure 12). On average, this trend was consistent across the three slopes; however, depending on the windflow model, the fraction of seasonal blowing snow transport during this 12 hour period varied by as much as 20%. Conversely, less than 1% of the cumulative seasonal snow transport was simulated to occur more than 72-hours after a snowfall. The windflow model choice had a lesser impact on the timing of sublimation losses. It is interesting to note that >90% of the seasonal blowing snow sublimation losses and <55% of the

surface sublimation losses were simulated to occur within 36 hours of snowfall (Figure 12), with the most surface sublimation occurring during the melt season (>72 hours).

4. Discussion

When forced with ridgetop windflow observations, all three windflow models adequately captured the general pattern of high wind speeds on the exposed windward side of the alpine ridge and lower wind speeds on the protected leeward side. The perpendicular nature of the prevailing wind direction recorded at Fisera Ridge was remarkably persistent (Figure 2) as a combined result of local terrain orientation and regional flow patterns. The slope-parallel windflow persistence likely facilitated model accuracy by placing less emphasis on model skill at simulating windflow direction relative to the reference station, and more emphasis on wind velocity representation. As such, the model comparison represents a 'best-case' scenario that provides important insight into the impacts of windflow calculations on simulations of alpine snow redistribution and ablation.

Compared to measurements, the MS turbulence model had the greatest bias on both slopes and highest RMSE on the windward slope (Figure 4). As previously noted, the empirical LS windflow model weighting factors *upwind slope* and *curvature* were not determined from local calibration, but specified as in previous empirical studies to be more consistent with how an empirical windflow model might be applied to complex terrain. Despite the lack of local calibration, when compared to measured wind speed on the two slopes the empirical LS model performed as well as the WS model (in terms of the RMSE values) and better than the MS model. For example, the MS simple turbulence model had the greatest average wind speed bias of -0.95 m s^{-1} compared to the relatively smaller biases of the LS (0.25 m s^{-1}) and WS (0.05 m s^{-1}) windflow models (Figure 4). However, the windflow model evaluation against windward and leeward slope wind speeds was a poor indicator of how wind speed errors might propagate into DSM snow state errors and flux differences.

The three windflow models used to force DSM had appreciable and varying impact on the calculation of seasonal snow mass balance (i.e., depth, SWE) and fluxes (i.e., transport, sublimation and melt). The two turbulence models resulted in the deepest snowpack (> 200 cm) in terrain-sheltered locations downwind of the ridgetop (Figures 7 and 8). By comparison, the LS-driven DSM simulated a smoothly varying snow-cover, deepest in proximity to the ridgetop and shallowest on both the windward and leeward slopes. The results suggest that improved performance of the empirical LS windflow model might have been obtained from reducing the distribution of weight on the curvature parameter and increasing the weight on the upwind slope parameter; however, there is no guarantee that calibration of LS against wind speed alone would have improved its performance in simulating the spatial distribution of SWE. The MS model resulted in the lowest snowpack depth and SWE errors on the windward slope and ridgetop and WS resulted in the lowest errors on the leeward slope (Figures 5 and 9; Table 1). These results contrast with the evaluation of wind speed simulations discussed previously and imply that,

particularly in high-wind environments such as the ridgetop and windward slope where MS was not the most accurate wind speed model, the representation of precisely how much the snow transport wind speed threshold was exceeded may be of secondary importance for snow transport calculations to the representation of wind speed spatial variability.

Modelled wind speed acceleration or deceleration indicated by positive and negative du/dx values, respectively, (Figure 6b) determines whether snow simulated at a grid element is scoured or deposited. The variation in the sign, magnitude, and spatial location of the simulated breaks in wind speed among the three models indicate substantial fine-scale differences in windflow representation (Figure 6b) that contribute to differences in the snow depth and SWE estimates (Figure 6c). The smoothly varying snow-cover simulated by the LS-driven DSM is attributed to the low variation and small (absolute) values of the du/dx values estimated by the LS windflow model. By comparison, substantial variation in du/dx values simulated by the two turbulence windflow models resulted in higher variability in simulated SWE (Figure 6c). The results suggest that the turbulence models can represent windflow (and SWE) variability at two scales: i) slope-scale terrain effects such as the windward and leeward sides of a ridge, and ii) small-scale (i.e., < 10 m) effects of slight terrain undulations. Differences in the exact position of wind speed breaks over the ridge simulated by the turbulence models are likely due to structural disparities between the linear (MS) and nonlinear (WS) windflow models. The empirical LS model may have been able to capture these micro-scale wind speed variations with a smaller length-scale curvature parameter, but such a parameter change may come at the expense of reduced slope-scale accuracy, i.e., the curvature metric would then be more sensitive to small-scale terrain features than slope-scale features such as the ridge. While overall errors in estimating snow depth and SWE were generally smallest using either of the two turbulence windflow models compared to the empirical model (Table 1), the ability of WS to estimate the leeward slope drift is notable for two reasons: the snowpack mass balance at Fisera Ridge is dependent upon accurately simulating upwind snow transport and in-transit sublimation; and the estimation of hydrologically important leeward drifts is one of the main reasons to run a blowing snow model.

The models evaluated here assume that the wind direction is constant for all grid elements for a given time step and do not consider terrain-induced alterations to the windflow direction. In locations where the wind direction varies little and topography is simple, such as Fisera Ridge, the computational efficiency of assuming a constant wind direction may outweigh potential deficiencies in model performance due to the assumption. When wind direction over a domain is unknown and terrain is more complex, then windflow patterns should be estimated based on terrain characteristics (e.g., Ryan, 1977) or within a turbulence (e.g., Essery *et al.*, 1999) or atmospheric (e.g., Mott *et al.*, 2014) model. Errors in the simulated drift formation compared to measurements can accrue from the steady state assumption of the blowing snow model which does not include a realistic temporal and spatial lag in the formation of snow deposition features after a drop in wind speed on a lee slope. Non-steady-state blowing snow models are in their infancy due to an incomplete understanding of turbulent snow particle interactions in complex

terrain. Despite these challenges, for the general application to areas of limited terrain complexity such as presented here, the DSM results suggest that the more physically realistic turbulence models are an example of warranted model complexity over the empirical LS windflow model.

It is shown that cumulative seasonal snow transport and sublimation losses can be significant and are sensitive to the windflow characterization. When averaged over the ridge, the cumulative seasonal blowing snow sublimation losses relative to seasonal snowfall simulated by DSM when forced with the MS (19%) and WS (17.5%) windflow models were similar to estimates in MacDonald et al. (2010) (19%); note that the empirical LS windflow model caused substantially lower estimates of blowing snow losses (10.5% of seasonal snowfall). The differences imply that the windflow model choice can have significant implications on slope-scale hydrology, ecology, and land surface representation; topics that require accurate characterization of snow-cover duration and snow drift magnitude.

The largest blowing snow event of the 2008 winter was accompanied by increases in both the 2.3 m air temperature and saturation deficit (Figure 11). The observations support previous multi-height measurements made at a Canadian Prairie site (Pomeroy (1988) as reported in Pomeroy and Li (2000)) where the process was attributed to dry air advection that resulted from the mixing of initially stable boundary layers. The field examples suggest that atmospheric boundary layer models must consider more thermodynamic phenomena than the negative feedback process (Pomeroy and Li, 2000), particularly in wind-prone complex terrain such as the Canadian Rocky Mountains. Future development of fully coupled atmospheric and blowing snow models, validated by multi-height field observation, may provide useful insight into the relative and often compensatory roles of blowing snow sublimation, moisture and temperature feedback, and dry air advection mechanisms.

DSM estimated that the majority of cumulative seasonal snow transport and blowing snow sublimation occurred in the 13 – 24 hour period after a storm event (Figure 12), illustrating the importance of considering blowing snow threshold conditions and in-transit sublimation in calculating snow redistribution. The results raise questions about how simple snow redistribution models that immediately reallocate snowfall (e.g., Winstral and Marks, 2002) without considering in-transit sublimation might result in the propagation of SCA and sublimation errors. The accurate characterization of SCA is required to simulate the surface albedo, temperature, and energy balance that are important for models that simulate atmospheric and hydrological dynamics (Shook *et al.*, 1993; Pomeroy *et al.*, 1998). For example, the windflow model used to force DSM impacted the simulation of late-lying snow patches known to enhance alpine albedo and provide meltwater to alpine and subalpine lakes, wetlands and streams (Elder *et al.*, 1991). During the spring and summer, water availability in alpine landscapes is influenced by winter snow drift patterns, which in turn critically impacts vegetation distribution (Billings and Bliss, 1959; Walker *et al.*, 2001), soil moisture (Taylor and Seastedt, 1994), contaminant loading (Pomeroy *et al.*, 1991) and nutrient cycling (Williams and Melack, 1991). At the slope-scale in

515 complex terrain, distributed blowing snow models require realistic windflow models to
516 accurately simulate these ecohydrological processes.

517 Finally, when DSM snow mass fluxes were spatially aggregated to include a larger area (~1
518 km^2), which included less wind-prone areas, the windflow model-related differences in the time
519 evolution of aggregated snow transport and melt were subtle to negligible; however, there were
520 appreciable differences in sublimation and snow-cover depletion. The low sensitivity of
521 simulated spring melt fluxes to the windflow calculations may be underestimated but the error is
522 difficult to quantify due to the uncertainty in advection parameterisations for complex terrain
523 snowmelt calculations. While not considered here, turbulent advection of sensible heat can
524 influence snow-cover depletion rates (Shook *et al.*, 1993; Mott *et al.*, 2014). Turbulent advection
525 on Fisera Ridge is considered to be relatively small because while snow-cover is rapidly depleted
526 on the windward slope and ridgetop it persists in a large, continuous drift on the leeward slope
527 leading to one large snow patch with one leading edge. Thus, the spring snow-cover depletion
528 patterns at Fisera Ridge differ from the patchy snowpack with a wide distribution of snow patch
529 sizes and fetch lengths that have been studied in the Canadian Prairies or Arctic (Shook *et al.*,
530 1993; Granger *et al.*, 2002). The driving meteorological data for DSM was collected at a ridgetop
531 station that would be over snowcover when the entire domain was snow-covered and mostly
532 snow-free when only the leeward slope snowcover remained and so may have inherently
533 included some advected energy. While not explicitly considered, any additional turbulent energy
534 from advection may have propagated the reported differences in the estimated end-of-winter
535 SWE distribution amongst the windflow model-forced snow simulations due to inherent
536 feedback processes between SCA and the advection of sensible heat (Marsh and Pomeroy,
537 1996). Therefore, windflow model choice may have more influence on late-spring snow-cover
538 depletion rates and the time evolution of spatially aggregated spring snowmelt than reported
539 here.

540 The results suggest that the issue of warranted model complexity should be weighed in
541 careful consideration of the processes of interest, the model used, and the modelling objectives.
542 The variability of aggregated snow states, mass fluxes and SCA amongst windflow model-driven
543 DSM runs over landscape units corresponding to the windward, ridgetop and leeward slopes in
544 Figure 10 is substantial and suggests that improved simulations at the landscape unit scale can be
545 gained by using turbulence-based windflow models.

546 **5. Conclusions**

547 Compared to automated and manual measurements made on opposing sides of an alpine ridge,
548 DSM forced by the three windflow models produced distinct differences in the seasonal
549 evolution, magnitude and location of simulated snow drifts. The empirical LS-driven DSM
550 simulated a smoothly varying snow-cover, deepest in close proximity to the ridge crest and
551 shallowest on both the windward and leeward slopes. This was in contrast to the general
552 understanding of snow accumulation around alpine ridges. By comparison, the two turbulence
553 windflow model-driven DSM runs simulated snow-cover patterns that were similar to the

LiDAR-derived snow-cover with shallower snow and snow-free areas on the windward and ridgetop zones, and a deeper drift covering much of the leeward slope. DSM forced by the two turbulence models simulated the deepest snowpack (> 200 cm) in roughly similar locations. The WS-driven DSM provided the most accurate snow simulation on the leeward slopes where large drifts accumulate due to snow transport from upwind slopes. On average, cumulative surface sublimation losses were approximately 50% of the cumulative blowing snow sublimation losses, which were 19% and 17.5% of the cumulative seasonal snowfall with the MS and WS turbulence models, but only 10.5% with the LS empirical windflow model. Strong seasonality was detected in the sublimation source; blowing snow sublimation generally ceased at the beginning of March, while most of the seasonal surface sublimation occurred from March through July. The location of the greatest (total) sublimation losses was windflow model-dependent: sublimation was highest on the windward slope with the LS- and WS-driven DSM, but on the ridgetop with the MS-driven DSM. The results show that the windflow model choice can have significant implications for calculating snow regimes and all snow mass fluxes at point- to slope-scales that are important for alpine ecology and at landscape scales relevant to hydrological and climate models that consider sub-grid or sub-basin variability.

ACKNOWLEDGEMENTS

Financial support was provided by NSERC, CRC, CERC, CFI, and AESRD. The authors thank C. Hopkinson, Nakiska Mountain Resort, the University of Calgary Biogeoscience Institute, Centre for Hydrology students and staff, and two anonymous reviewers..

REFERENCES

Bernhardt M, Zängl G, Liston G, Strasser U, Mauser W. 2009. Using wind fields from a high-resolution atmospheric model for simulating snow dynamics in mountainous terrain. Hydrological processes, **23**: 1064-1075.

Best M, Pryor M, Clark D, Rooney G, Essery R, Ménard C, Edwards J, Hendry M, Porson A, Gedney N. 2011. The Joint UK Land Environment Simulator (JULES), model description–Part 1: energy and water fluxes. Geoscientific Model Development, **4**: 677-699.

Billings WD, Bliss L. 1959. An alpine snowbank environment and its effects on vegetation, plant development, and productivity. Ecology: 388-397.

Bowling L, Pomeroy J, Lettenmaier D. 2004. Parameterization of blowing-snow sublimation in a macroscale hydrology model. Journal of Hydrometeorology, **5**: 745-762.

Brooks PD, Williams MW. 1999. Snowpack controls on nitrogen cycling and export in seasonally snow-covered catchments. Hydrological Processes, **13**: 2177-2190.

Dadic R, Mott R, Lehning M, Burlando P. 2010. Wind influence on snow depth distribution and accumulation over glaciers. Journal of Geophysical Research: Earth Surface (2003–2012), **115**.

Dornes PF, Pomeroy JW, Pietroniro A, Carey SK, Quinton WL. 2008. Influence of landscape aggregation in modelling snow-cover ablation and snowmelt runoff in a sub-arctic mountainous environment. Hydrological Sciences Journal, **53**: 725-740.

Dyunin AK. 1959. Fundementals of the Theory of Snow Drifting. Izvest. Sibirsk, Otdel. Akad. Nauk. U.S.S.R., **12**: 11-24.

Egli L, Jonas T, Grünewald T, Schirmer M, Burlando P. 2012. Dynamics of snow ablation in a small Alpine catchment observed by repeated terrestrial laser scans. Hydrological Processes, **26**: 1574-1585.
Elder K, Dozier J, Michaelsen J. 1991. Snow accumulation and distribution in an alpine watershed. Water Resources Research, **27**: 1541-1552.
Essery R, Li L, Pomeroy J. 1999. A distributed model of blowing snow over complex terrain. Hydrological processes, **13**: 2423-2438.
Essery R, Pomeroy J. 2004. Vegetation and topographic control of wind-blown snow distributions in distributed and aggregated simulations for an Arctic tundra basin. Journal of Hydrometeorology, **5**: 735-744.
Fang X, Pomeroy J. 2009. Modelling blowing snow redistribution to prairie wetlands. Hydrological processes, **23**: 2557-2569.
Granger R, Pomeroy J, Parviainen J. 2002. Boundary-layer integration approach to advection of sensible heat to a patchy snow cover. Hydrological Processes, **16**: 3559-3569.
Gravdahl AR, Vargvei N. 1998. Meso scale modeling with a reynolds averaged navier-stokes solver: assessment of wind resources along the Norwegian coast. In: 31th IEA experts meeting. State of the Art on Wind Resource Estimation.
Greene EM, Liston GE, Pielke Sr RA. 1999. Simulation of above treeline snowdrift formation using a numerical snow-transport model. Cold Regions Science and Technology, **30**: 135-144.
Grunewald T, Schirmer M, Mott R, Lehning M. 2010. Spatial and temporal variability of snow depth and ablation rates in a small mountain catchment. Cryosphere, **4**: 215-225.
Hopkinson C, Pomeroy J, Debeer C, Ellis C, Anderson A. 2012. Relationships between snowpack depth and primary LiDAR point cloud derivatives in a mountainous environment. In: IAHS-AISH publication, pp: 354-358.
Jackson P, Hunt J. 1975. Turbulent wind flow over a low hill. Quarterly Journal of the Royal Meteorological Society, **101**: 929-955.
Launder BE, Spalding D. 1974. The numerical computation of turbulent flows. Computer methods in applied mechanics and engineering, **3**: 269-289.
Lehning M, Lˆwe H, Ryser M, Raderschall N. 2008. Inhomogeneous precipitation distribution and snow transport in steep terrain. Water Resour. Res., **44**: W07404. DOI: 10.1029/2007wr006545.
Li L, Pomeroy JW. 1997. Estimates of threshold wind speeds for snow transport using meteorological data. Journal of Applied Meteorology, **36**: 205-213.
Liston GE, Elder K. 2006. A Meteorological Distribution System for High-Resolution Terrestrial Modeling (MicroMet). Journal of Hydrometeorology, **7**: 217-234. DOI: 10.1175/jhm486.1.
Liston GE, Sturm M. 1998. A snow-transport model for complex terrain. Journal of Glaciology, **44**: 498-516.
MacDonald M, Pomeroy J, Pietroniro A. 2010. On the importance of sublimation to an alpine snow mass balance in the Canadian Rocky Mountains. Hydrology and Earth System Sciences, **14**: 1401-1415.
Male D, Granger R. 1981. Snow surface energy exchange. Water Resources Research, **17**: 609-627.
Marks D, Dozier J. 1992. Climate and energy exchange at the snow surface in the Alpine Region of the Sierra Nevada: 2. Snow cover energy balance. Water Resources Research, **28**: 3043-3054.
Marks D, Winstral A. 2001. Comparison of snow deposition, the snow cover energy balance, and snowmelt at two sites in a semiarid mountain basin. Journal of Hydrometeorology, **2**: 213-227.
Marsh P, Pomeroy J. 1996. Meltwater fluxes at an arctic forest-tundra site. Hydrological Processes, **10**: 1383-1400.
Mason P, Sykes R. 1979. Flow over an isolated hill of moderate slope. Quarterly Journal of the Royal Meteorological Society, **105**: 383-395.

640 Mott R, Faure F, Lehning M, Lowe H, Hynek B, Michlmayr G, Prokop A, Schoner W. 2008. Simulation of
641 seasonal snow cover distribution for glacierized sites (Sonnblick, Austria) with the Alpine3D
642 model. Annals of Glaciology, **49**: 155-160.
643 Mott R, Lehning M. 2010. Meteorological Modeling of Very High-Resolution Wind Fields and Snow
644 Deposition for Mountains. J Hydrometeorol, **11**: 934-949. DOI: 10.1175/2010jhm1216.1.
645 Mott R, Lehning M, Daniels M, Lehning M. 2014. Atmospheric Flow Development and Associated
646 Changes in Turbulent Sensible Heat Flux over a Patchy Mountain Snow Cover. Journal of
647 Hydrometeorology.
648 Mott R, Schirmer M, Bavay M, Grünewald T, Lehning M. 2010. Understanding snow-transport processes
649 shaping the mountain snow-cover. The Cryosphere, **4**: 545-559.
650 Ménard C, Essery R, Pomeroy J. 2014. Modelled sensitivity of the snow regime to topography, shrub
651 fraction and shrub height. Hydrology and Earth System Sciences Discussions, **11**: 223-263.
652 Ménard CB, Essery R, Pomeroy J, Marsh P, Clark DB. 2014. A shrub bending model to calculate the
653 albedo of shrub-tundra. Hydrological Processes, **28**: 341-351.
654 Pohl S, Marsh P, Liston G. 2006. Spatial-temporal variability in turbulent fluxes during spring snowmelt.
655 Arctic, Antarctic, and Alpine Research, **38**: 136-146.
656 Pomeroy J. 1989. A process-based model of snow drifting. Ann. Glaciol, **13**: 237-240.
657 Pomeroy J, Davies T, Tranter M. 1991. The impact of blowing snow on snow chemistry. In: Seasonal
658 Snowpacks, Springer, pp: 71-113.
659 Pomeroy J, Gray D. 1995. Snowcover accumulation, relocation and management. Bulletin of the
660 International Society of Soil Science no, **88**.
661 Pomeroy J, Gray D, Landine P. 1993. The prairie blowing snow model: characteristics, validation,
662 operation. Journal of Hydrology, **144**: 165-192.
663 Pomeroy J, Li L. 2000. Prairie and Arctic areal snow cover mass balance using a blowing snow model.
664 Journal of Geophysical Research: Atmospheres (1984–2012), **105**: 26619-26634.
665 Pomeroy J, Toth B, Granger R, Hedstrom N, Essery R. 2003. Variation in surface energetics during
666 snowmelt in a subarctic mountain catchment. Journal of Hydrometeorology, **4**: 702-719.
667 Pomeroy JW. 1988. Wind transport of snow. University of Saskatchewan, pp: 226.
668 Pomeroy JW, Gray DM, Shook KR, Toth B, Essery RLH, Pietroniro A, Hedstrom N. 1998. An evaluation of
669 snow accumulation and ablation processes for land surface modelling. Hydrological Processes,
670 **12**: 2339-2367. DOI: 10.1002/(sici)1099-1085(199812)12:15<2339::aid-hyp800>3.0.co;2-l.
671 Pomeroy JW, Marsh P, Gray DM. 1997. Application of a distributed blowing snow model to the Arctic.
672 Hydrological Processes, **11**: 1451-1464.
673 Ryan BC. 1977. A mathematical model for diagnosis and prediction of surface winds in mountainous
674 terrain. Journal of Applied Meteorology, **16**: 571-584.
675 Schirmer M, Wirz V, Clifton A, Lehning M. 2011. Persistence in intra-annual snow depth distribution: 1.
676 Measurements and topographic control. Water Resources Research, **47**.
677 Schmidt R. 1972. Sublimation of wind-transported snow--a model. USDA Forest Service research paper
678 RM-United States, Rocky Mountain Forest and Range Experiment Station.
679 Schmidt R. 1986. Transport rate of drifting snow and the mean wind speed profile. Boundary-Layer
680 Meteorology, **34**: 213-241.
681 Shook K, Gray D, Pomeroy J. 1993. Temporal variation in snowcover area during melt in prairie and
682 alpine environments. Nordic Hydrology, **24**: 183-183.
683 Taylor P, Walmsley J, Salmon J. 1983. A simple model of neutrally stratified boundary-layer flow over
684 real terrain incorporating wavenumber-dependent scaling. Boundary-Layer Meteorology, **26**:
685 169-189.
686 Taylor R, Seastedt T. 1994. Short-and long-term patterns of soil moisture in alpine tundra. Arctic and
687 Alpine Research: 14-20.

Walker D, Billings W, De Molenaar J. 2001. Snow–vegetation interactions in tundra environments. Snow ecology: an interdisciplinary examination of snow-covered ecosystems: 266-324.
Wallace JM, Hobbs PV. 2006. Atmospheric science: an introductory survey. Academic press.
Walmsley J, Taylor P, Keith T. 1986. A simple model of neutrally stratified boundary-layer flow over complex terrain with surface roughness modulations (MS3DJH/3R). Boundary-Layer Meteorology, **36**: 157-186.
Walmsley JL, Salmon J, Taylor P. 1982. On the application of a model of boundary-layer flow over low hills to real terrain. Boundary-Layer Meteorology, **23**: 17-46.
Williams MW, Melack JM. 1991. Solute chemistry of snowmelt and runoff in an alpine basin, Sierra Nevada. Water resources research, **27**: 1575-1588.
Winstral A, Marks D. 2002. Simulating wind fields and snow redistribution using terrain-based parameters to model snow accumulation and melt over a semi-arid mountain catchment. Hydrological Processes, **16**: 3585-3603.
Wipf S, Stoeckli V, Bebi P. 2009. Winter climate change in alpine tundra: plant responses to changes in snow depth and snowmelt timing. Climatic Change, **94**: 105-121.
Yang J, Yau M, Fang X, Pomeroy J. 2010. A triple-moment blowing snow-atmospheric model and its application in computing the seasonal wintertime snow mass budget. Hydrology and Earth System Sciences, **14**: 1063-1079.

Table 1. Snow depth and SWE errors for the snow simulations forced by the three windflow models as evaluated against snow observations made at the three stations. The shaded cells indicate the windflow model that produced the lowest error values for each station. Note that the depth errors were calculated from mean daily automated measurements while the SWE errors were the average error values computed on manual observations at near each station during 13 repeated snow surveys.

		RMSE			bias		
		windward	ridgetop	leeward	windward	ridgetop	leeward
Depth, cm	LS	22.1	83.4	53.7	16.6	73.9	-38.9
	MS	14.4	9.3	38.1	7.5	3.5	-22.7
	WS	29.3	25.7	27.0	21.4	20.9	-10.0
SWE, mm	LS	91	429	270	70	419	-259
	MS	57	38	170	37	11	-157
	WS	131	110	84	97	101	-66

716 FIGURE CAPTIONS

717 Figure 1: Study site map showing the nested model domains (24 km x 24 km with 150 m
718 elevation contour lines; 1.024 km x 1.024 km with 10 m elevation contour lines) centred on the
719 locations of three meteorological stations on the alpine Fisera Ridge in the Marmot Creek
720 Research Basin, Alberta, Canada (location indicated by the star in the upper-right panel). The
721 small maps at right (20 m elevation contour lines) indicate the (top): LiDAR-derived roughness
722 length values over the inner domain and (bottom): the locations of the snow survey transects
723 relative to the three meteorological stations. Rectangular domains used to compare spatially
724 averaged simulated fluxes representative of the windward, ridgetop, and leeward parts of Fisera
725 Ridge are shown.

726 Figure 2: Wind roses including the mean and maxima wind speeds for the windward, ridgetop
727 and leeward stations from 15-minute averaged data collected from October, 2008 to September,
728 2010 (n=57,441). Analysis was limited to time-steps when data were available from all three
729 stations. Note that wind direction was only measured at the ridgetop station and was assumed
730 representative of the two other stations for the purposes of the wind rose comparison.

731 Figure 3: Scatter plots of wind speed comparing modelled values (y-axes) from each of the three
732 windflow models (panel rows) to measured values (x-axes) at the windward (left panels) and
733 leeward (right panels) automated weather stations. The (linear) regression fits, coefficients of
734 determination (R^2), and correlation coefficients (r) are indicated.

735 Figure 4: Mean (bars) and standard deviation (lines) of modelled wind speed RMSE (top) and
736 bias (bottom) for the three windflow models compared to measurements at the windward and
737 leeward automated weather stations.

738 Figure 5: Measured snow depth (top) and SWE (bottom) compared to simulated values from the
739 three windflow models (lines) at the windward (left panel column), ridgetop (centre panel
740 column), and leeward (right panel column) stations.

741 Figure 6: Modelled a) seasonal mean wind speed normalized by the ridgetop station
742 observations, b) the change in mean wind speed with distance (du/dx), and c) snow water
743 equivalent (SWE) presented as the pixel-wise nearest-neighbor mean (lines) and standard
744 deviation (shading) near the time of seasonal maximum accumulation (May 1, 2008) along d) a
745 160 m linear (12 m vertical) transect from the windward to leeward sides of the alpine ridge.

746 Figure 7: The LiDAR-measured snow depth on Fisera Ridge on 28 March, 2008 (left) compared
747 to that simulated by DSM forced by wind speed output from the Liston-Sturm (LS), Mason-
748 Sykes (MS) and Windsim (WS) windflow models. The location of the windward (red marker),
749 ridgetop (black marker), and leeward (blue marker) stations are indicated. The elevation contour
750 lines are included.

Figure 8: Distributed maps of SWE (color scale) near the Fisera Ridge stations (markers) on the dates of select snow surveys (panel rows) as simulated by DSM forced with output from the three windflow models (panel columns). Elevation contour lines are included.

Figure 9: Model SWE error computed as the mean (bars) and standard deviation (lines) of 'modelled - measured' SWE averaged along the snow survey transects for 13 surveys on the windward (left), ridgetop (centre), and leeward (right) sides of Fisera Ridge for the DSM model forced by wind speed output from the Liston-Sturm (LS), Mason-Sykes (MS) and Windsim (WS) windflow models.

Figure 10: Cumulative fluxes of snow transport, sublimation (total, surface and blowing snow losses), melt, and snow covered area averaged within domains centered on the windward, ridgetop, leeward, and the entire domain as simulated by DSM forced with wind speed output from the Liston-Sturm (LS), Mason-Sykes (MS) and Windsim (WS) windflow models for the 2007-2008 snow season.

Figure 11: Measured values of wind speed, air temperature, precipitation (left axis) and relative humidity (right axis) during a blowing snow event on February 29, 2008 at the Fisera Ridge (ridgetop) station. Blowing snow sublimation rates estimated by DSM forced with windflow output from the Windsim model at the locations of the windward, ridgetop and leeward stations are included. Photographs from a field camera mounted on the ridgetop station looking northwest toward the windward slope show snow cover before (15:00 Feb. 28) and after (12:00 Feb. 29) the blowing snow event.

Figure 12: The timing of normalized (left y-axes) and cumulative (right y-axes) hourly seasonal snow transport and sublimation (total, surface and blowing snow) fluxes, binned in 12-hour intervals since the last snowfall (x-axes), as simulated by DSM forced by wind speed output from the Liston-Sturm (LS), Mason-Sykes (MS) and Windsim (WS) windflow models for the 2007-2008 snow season.

Table 1. Snow depth and SWE errors for the snow simulations forced by the three windflow models as evaluated against snow observations made at the three stations. The shaded cells indicate the windflow model that produced the lowest error values for each station. Note that the depth errors were calculated from mean daily automated measurements while the SWE errors were the average error values computed on manual observations at near each station during 13 repeated snow surveys.

		RMSE			bias		
		windward	ridgetop	leeward	windward	ridgetop	leeward
Depth, cm	LS	22.1	83.4	53.7	16.6	73.9	-38.9
	MS	14.4	9.3	38.1	7.5	3.5	-22.7
	WS	29.3	25.7	27.0	21.4	20.9	-10.0
SWE, mm	LS	91	429	270	70	419	-259
	MS	57	38	170	37	11	-157
	WS	131	110	84	97	101	-66

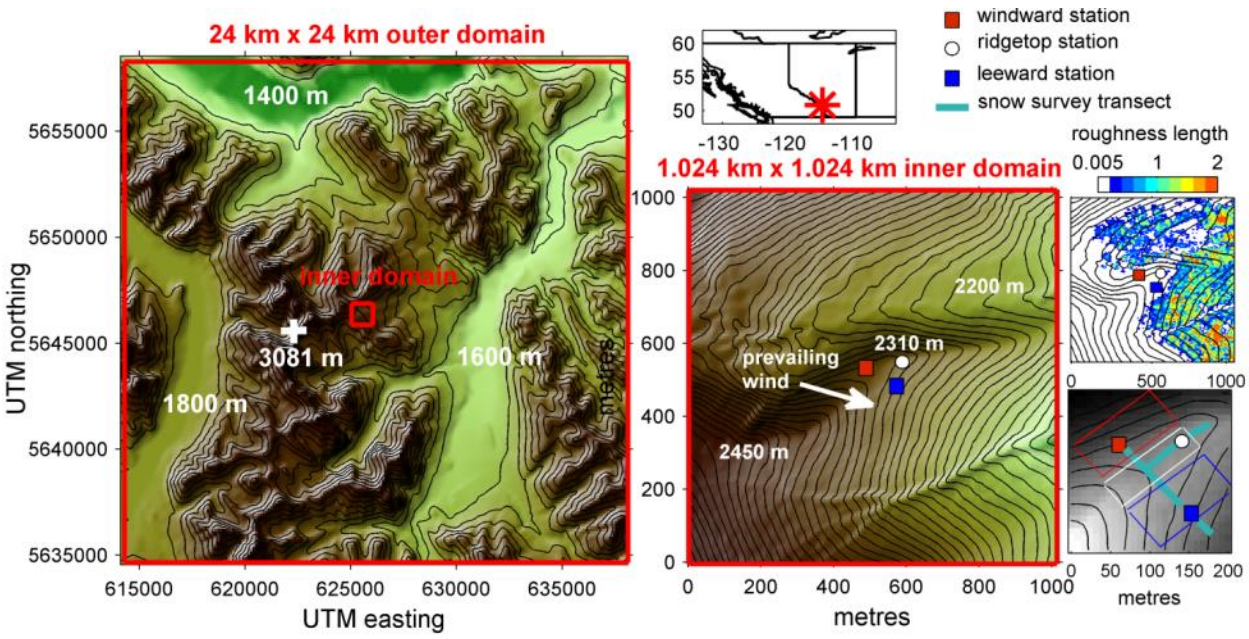

Figure 1: Study site map showing the nested model domains (24 km x 24 km with 150 m elevation contour lines; 1.024 km x 1.024 km with 10 m elevation contour lines) centred on the locations of three meteorological stations on the alpine Fisera Ridge in the Marmot Creek Research Basin, Alberta, Canada (location indicated by the star in the upper-right panel). The small maps at right (20 m elevation contour lines) indicate the (top): LiDAR-derived roughness length values over the inner domain and (bottom): the locations of the snow survey transects relative to the three meteorological stations. Rectangular domains used to compare spatially averaged simulated fluxes representative of the windward, ridgetop, and leeward parts of Fisera Ridge are shown.

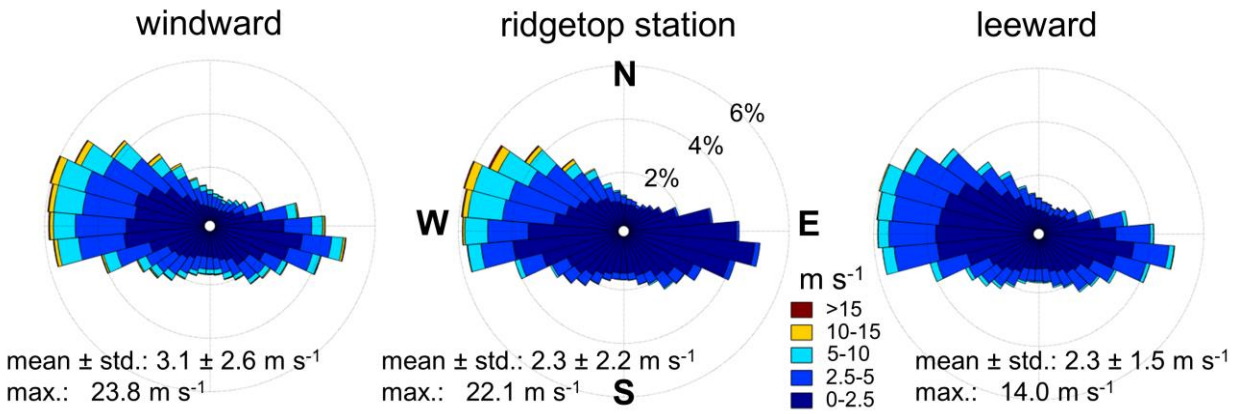

794

795 Figure 2: Wind roses including the mean and maxima wind speeds for the windward, ridgetop
796 and leeward stations from 15-minute averaged data collected from October, 2008 to September,
797 2010 (n=57,441). Analysis was limited to time-steps when data were available from all three
798 stations. Note that wind direction was only measured at the ridgetop station and was assumed
799 representative of the two other stations for the purposes of the wind rose comparison.

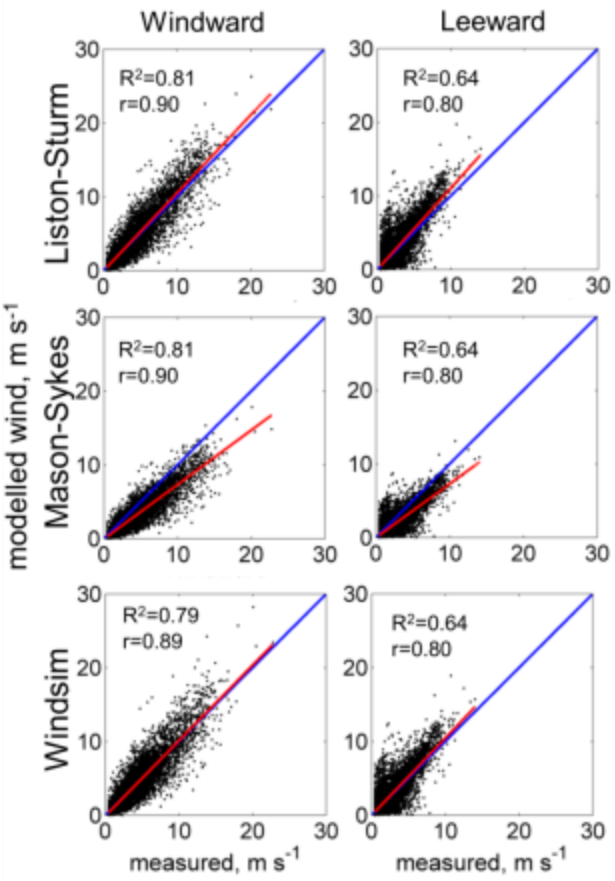

Figure 3: Scatter plots of wind speed comparing modelled values (y-axes) from each of the three windflow models (panel rows) to measured values (x-axes) at the windward (left panels) and leeward (right panels) automated weather stations. The (linear) regression fits, coefficients of determination (R^2), and correlation coefficients (r) are indicated.

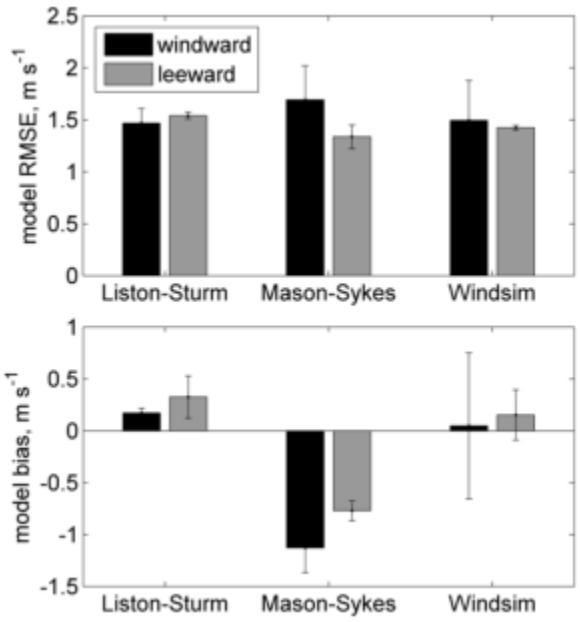

Figure 4: Mean (bars) and standard deviation (lines) of modelled wind speed RMSE (top) and bias (bottom) for the three windflow models compared to measurements at the windward and leeward automated weather stations.

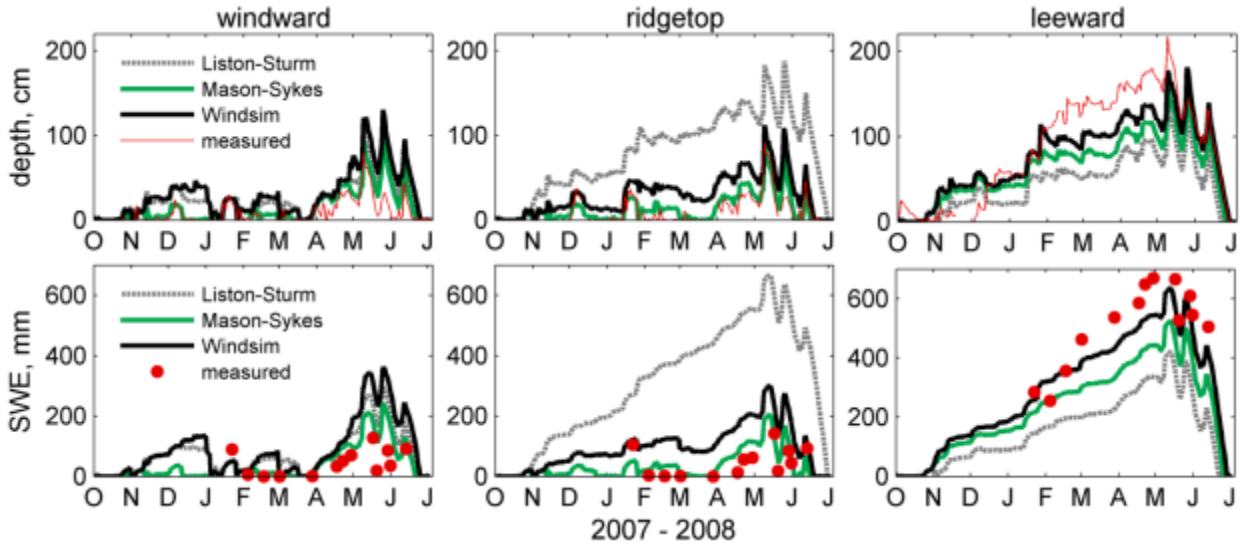

Figure 5: Measured snow depth (top) and SWE (bottom) compared to simulated values from the three windflow models (lines) at the windward (left panel column), ridgetop (centre panel column), and leeward (right panel column) stations.

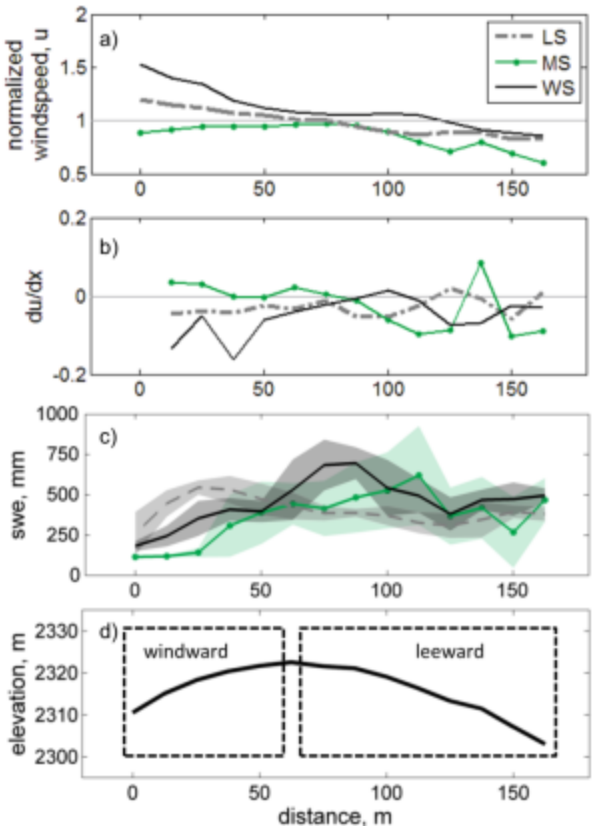

Figure 6: Modelled a) seasonal mean wind speed normalized by the ridgetop station observations, b) the change in mean wind speed with distance (du/dx), and c) snow water equivalent (SWE) presented as the pixel-wise nearest-neighbor mean (lines) and standard deviation (shading) near the time of seasonal maximum accumulation (May 1, 2008) along d) a 160 m linear (12 m vertical) transect from the windward to leeward sides of the alpine ridge.

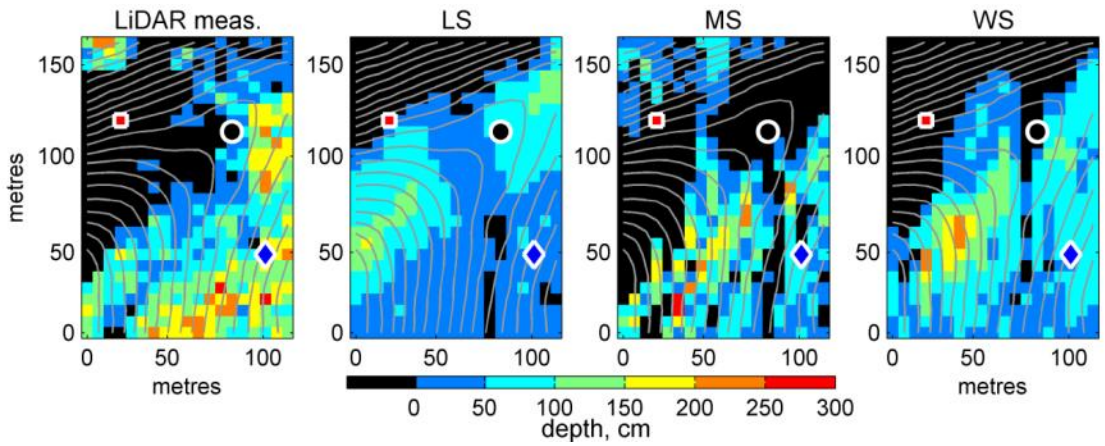

821

822 Figure 7: The LiDAR-measured snow depth on Fisera Ridge on 28 March, 2008 (left) compared
823 to that simulated by DSM forced by wind speed output from the Liston-Sturm (LS), Mason-
824 Sykes (MS) and Windsim (WS) windflow models. The location of the windward (red marker),
825 ridgetop (black marker), and leeward (blue marker) stations are indicated. The elevation contour
826 lines are included.

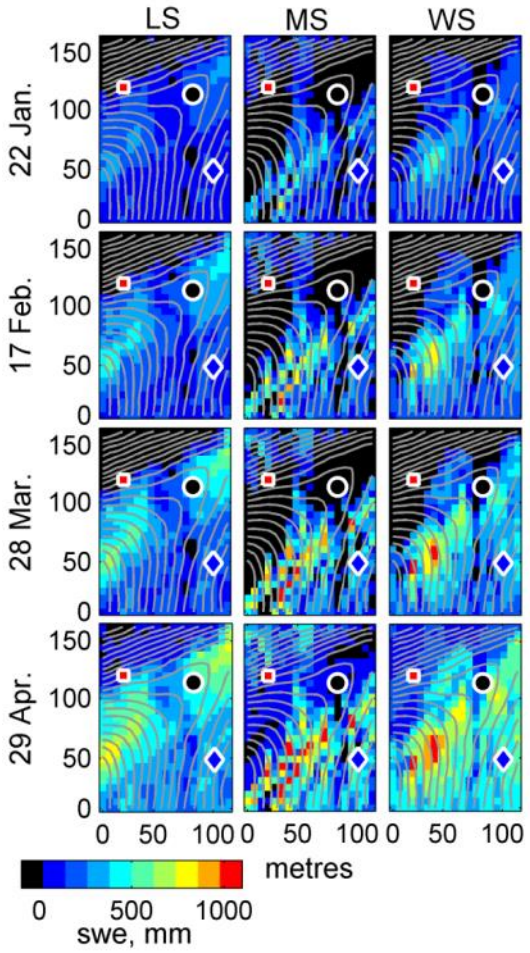

Figure 8: Distributed maps of SWE (color scale) near the Fisera Ridge stations (markers) on the dates of select snow surveys (panel rows) as simulated by DSM forced with output from the three windflow models (panel columns). Elevation contour lines are included.

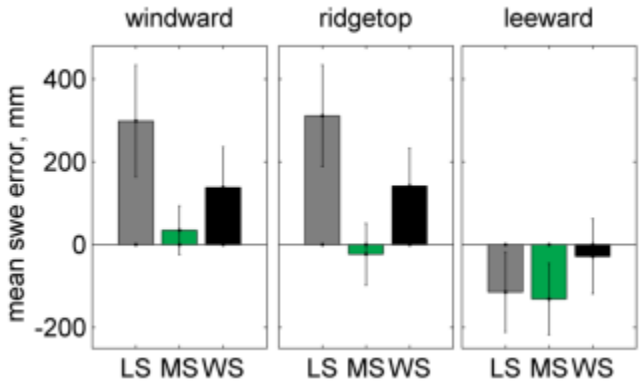

Figure 9: Model SWE error computed as the mean (bars) and standard deviation (lines) of 'modelled - measured' SWE averaged along the snow survey transects for 13 surveys on the windward (left), ridgetop (centre), and leeward (right) sides of Fisera Ridge for the DSM model forced by wind speed output from the Liston-Sturm (LS), Mason-Sykes (MS) and Windsim (WS) windflow models.

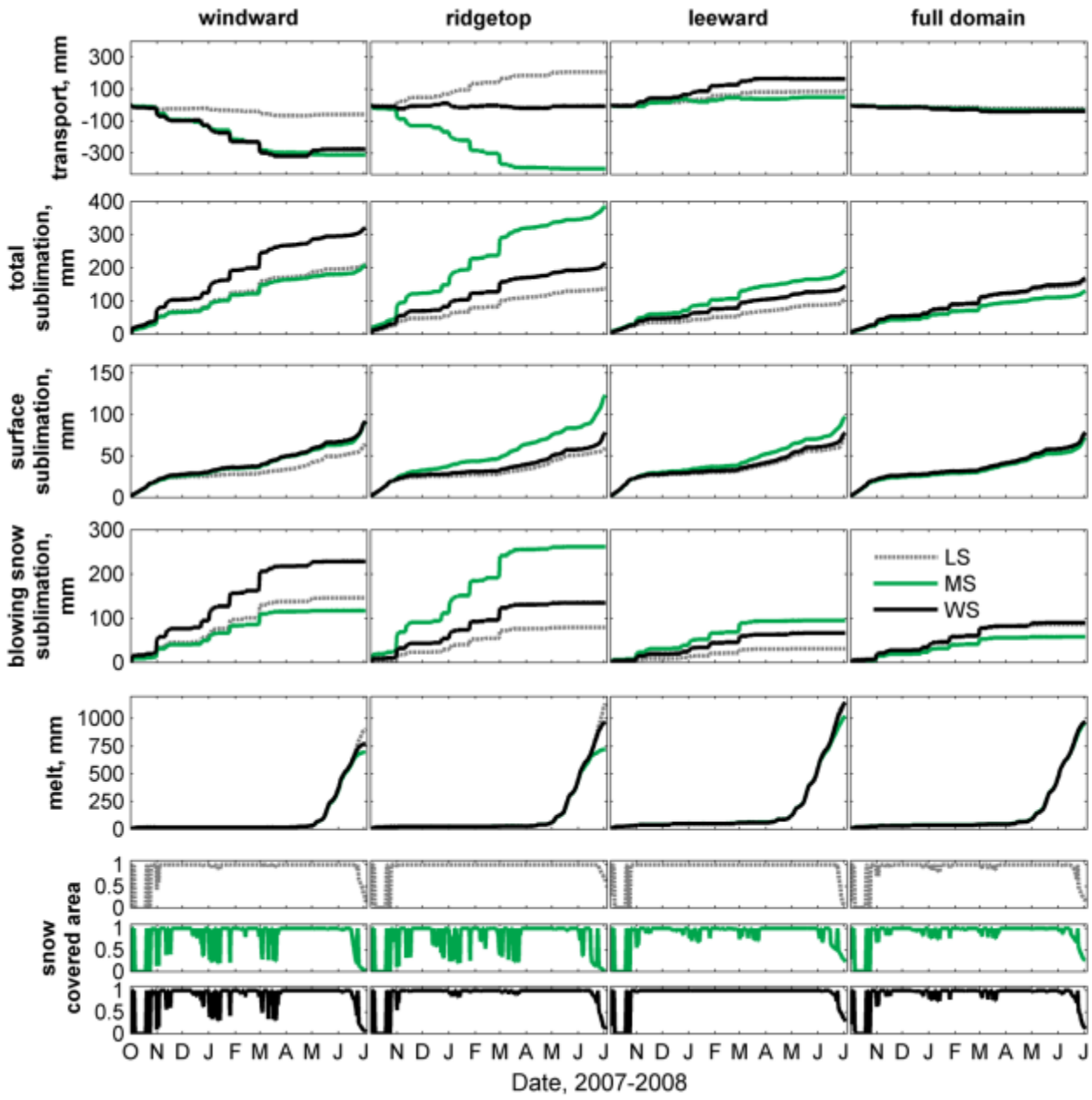

838

839 Figure 10: Cumulative fluxes of snow transport, sublimation (total, surface and blowing snow
840 losses), melt, and snow covered area averaged within domains centered on the windward,
841 ridgetop, leeward, and the entire domain as simulated by DSM forced with wind speed output
842 from the Liston-Sturm (LS), Mason-Sykes (MS) and Windsim (WS) windflow models for the
843 2007-2008 snow season.

844

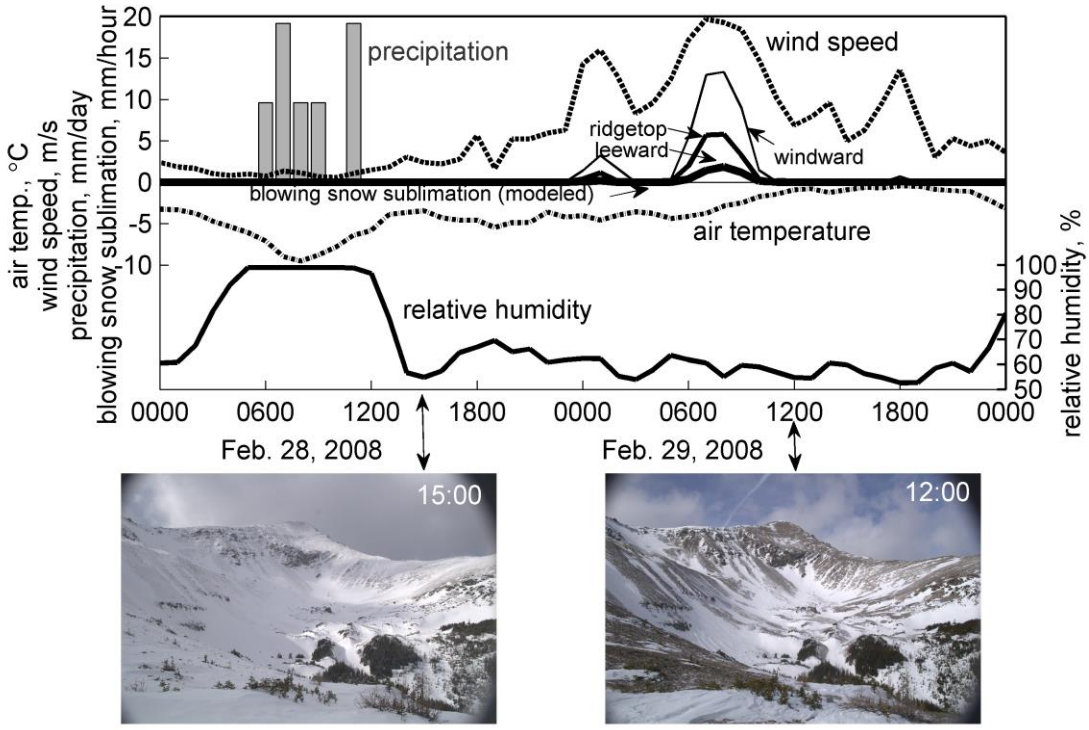

Figure 11: Measured values of wind speed, air temperature, precipitation (left axis) and relative humidity (right axis) during a blowing snow event on February 29, 2008 at the Fisera Ridge (ridgetop) station. Blowing snow sublimation rates estimated by DSM forced with windflow output from the Windsim model at the locations of the windward, ridgetop and leeward stations are included. Photographs from a field camera mounted on the ridgetop station looking northwest toward the windward slope show snow cover before (15:00 Feb. 28) and after (12:00 Feb. 29) the blowing snow event.

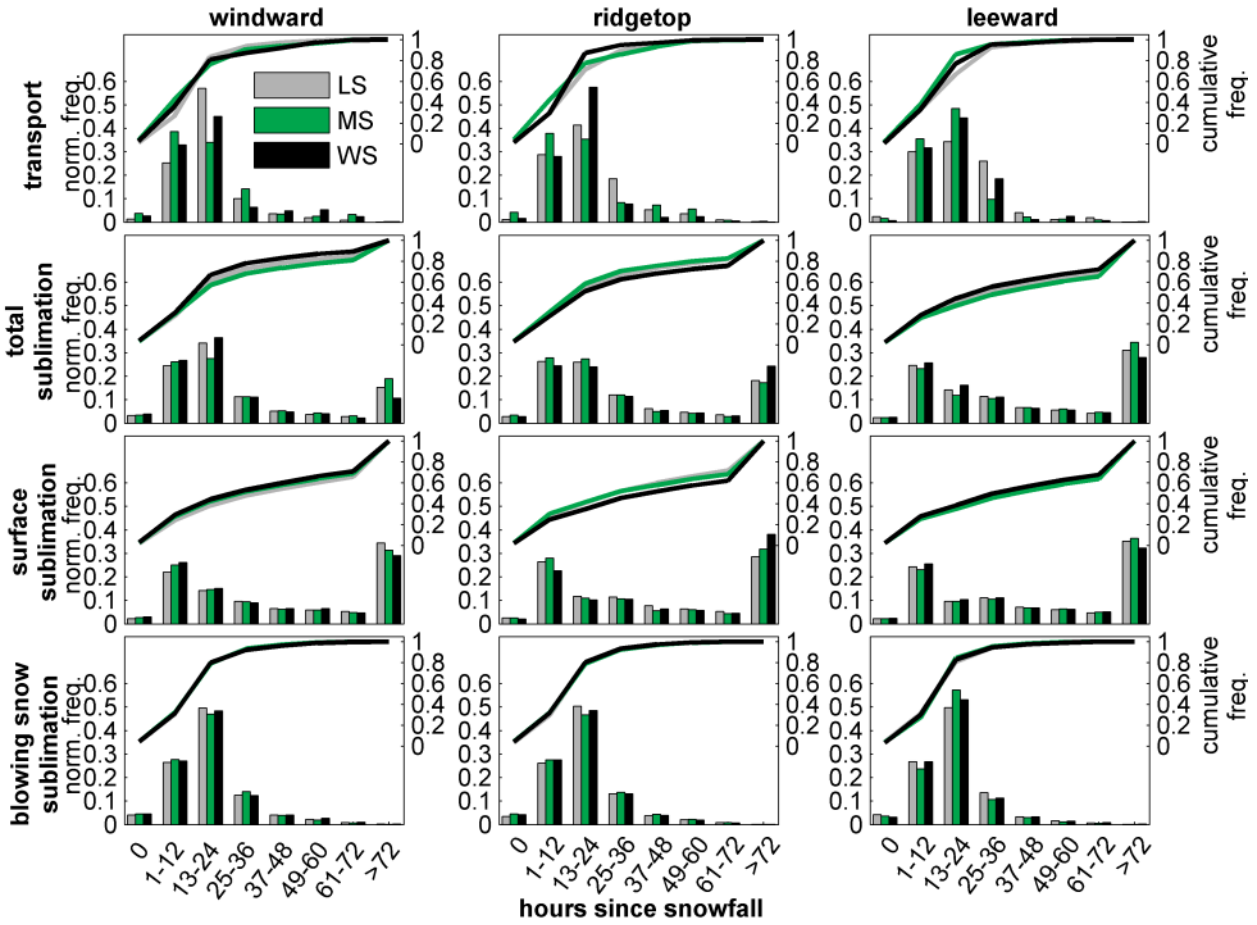

853

854 Figure 12: The timing of normalized (left y-axes) and cumulative (right y-axes) hourly seasonal
855 snow transport and sublimation (total, surface and blowing snow) fluxes, binned in 12-hour
856 intervals since the last snowfall (x-axes), as simulated by DSM forced by wind speed output
857 from the Liston-Sturm (LS), Mason-Sykes (MS) and Windsim (WS) windflow models for the
858 2007-2008 snow season.

859